




PAPER

A variable refractive index sensor based on epsilon-near-zero spatial selection structure and its potential in biological detection

Bao-Fei Wan¹, Hai-Ning Ye¹, Dan Zhang² and Haifeng Zhang^{1,*} ¹ College of Electronic and Optical Engineering, & College of Flexible Electronics (Future Technology), Nanjing University of Posts and Telecommunications, Nanjing, People's Republic of China² College of Information Science and Technology, Nanjing Forestry University, Nanjing 210037, People's Republic of China

* Author to whom any correspondence should be addressed.

E-mail: hanlor@163.com**Keywords:** spatially selective structure, epsilon-negative materials, refractive index, biosensor

RECEIVED

23 July 2022

REVISED

17 January 2023

ACCEPTED FOR PUBLICATION

25 January 2023

PUBLISHED

6 February 2023

Original content from
this work may be used
under the terms of the
[Creative Commons
Attribution 4.0 licence](https://creativecommons.org/licenses/by/4.0/).

Any further distribution
of this work must
maintain attribution to
the author(s) and the title
of the work, journal
citation and DOI.

**Abstract**

In this paper, a spatially selective (SS) structure is investigated through the critical jump characteristic when the permittivity of the epsilon-negative (ENG) materials approaches zero. In the range where the incident frequency of the TE wave is 5.1–5.6 c d^{-1} and that of the TM wave is 5.0–5.7 c d^{-1} , the transmittance exceeds 0.85 and the squareness factor (SF) surpasses 0.9. By adjusting the electronic plasma frequency to affect the position of epsilon-near-zero (ENZ) frequency, a wide-angle control of the SS characteristic extent is produced. Using the fragility of the critical angle to the background analyte medium, a variable refractive index sensor is proposed. When the electronic plasma frequency is continuously altered, the analyte with the measurement range of 1.1–1.3, 1.3–1.5, 1.5–1.7, or 1.7–1.9 can be detected. The corresponding sensitivity is 57.1 degrees/RIU, 48.8 degrees/RIU, 40.0 degrees/RIU, or 32.8 degrees/RIU. The elongation in the thickness of ENG materials contributes to the improvement of the SF, executing the discrimination of *Vibrio cholera*, *E. coli*, and *Shigella flexneri*. The effects of losses on device performance are also briefly considered. Different from previous studies, the proposed SS selective structure adopts a new ENZ mechanism, can simplify the design of the structure to a certain extent and has a possibility in the design of highly sensitive sensors.

1. Introduction

Deliberate regulation of the basic properties of electromagnetic waves such as amplitude, phase, frequency, polarization, and angle has always been a dream goal of scholars [1–3]. The researches on the first four characteristics are very mature and have been put into practical applications. Nevertheless, the investigation of the spatial angle domain remains a scientific challenge [4–6], and it is worth investing substantially in resources. Polarization-independent angle selection devices with productive spatially selective (SS) function play an important role in the fields of antenna design [7–9], optical communication systems [10–13], and terahertz light source optimization [9]. Predecessors have done multitudinous explorations of the formation mechanism of SS devices [14–19]. Among them, the most competitive technology is the Brewster angle mode and the selective diffraction behavior of photonic crystals.

In 2014, according to the transmission principle of the TM wave under the Brewster angle, Shen *et al* [20] used the cascade techniques to complete a transmission window with a size of 8 degrees near an angle of 55 degrees. Unfortunately, this SS property is fixedly dependent on the polarization mode, and is by no means suitable for the TE wave. Four years later, Tanaka *et al* [21] relied on the dispersive wave vector characteristics of the one-dimensional photonic crystals structure to establish a high-throughput angle-selective transmission window that does not depend on the polarization mode. The experimental results were highly fitted with theoretical simulations, providing the possibility for large-scale applications. However, the structure possesses as many as dozens of layers, which requires high process requirements and lacks flexibility in SS capabilities. In 2018, Qu *et al* [22] proposed a material system based on anisotropic materials and

half-wave plates, realizing a polarization-independent wide-angle-selective structure, which is also a very interesting design. In 2021, Grineviciute *et al* [23] utilized the selective diffraction behavior of the two-dimensional photonic crystals to achieve a 2-degree low-pass spatial filtering window, but its filtering ability is slightly weak, and the squareness factor (SF) needs to be further improved. Existing technologies often have problems with polarization sensitivity, complex structures with too many layers, or low SF. Therefore, it is urgent to propose a new mechanism to overcome these defects.

In recent years, an artificial material with only negative permittivity or permeability has attracted much attention [24–26]. They are mainly divided into two types, respectively negative permittivity and positive permeability or negative permeability and positive permittivity, these two types of materials are also known as epsilon-negative media (ENG) and mu-negative media. The ENG material is opaque when the permittivity is negative compared to a material with a positive exponent and only supports the evanescent modes since wave vectors are imaginary. By adjusting the electronic plasma frequency, the epsilon-near-zero (ENZ) frequency can be flexibly tuned. Thanks to the jump phenomenon of transmission characteristics near the ENZ frequency, unparalleled characteristics are displayed, furnishing new ideas for the study of high-transmission devices [27–30]. As far as we know, most of the research currently stays in the frequency domain, and no scholars have employed the ENZ characteristics to form an effective adjustment to the spatial domain, actually, which is a quite efficient method to achieve angle modulation.

Among numerous sensing mechanisms, the angle sensing principle stands out by virtue of its easy observation, high sensitivity, and strong resolvability [31–38]. It has unique advantages in refractive index detection, biological sample detection, virus analysis, etc. With the increasing development of the industrial level, the problem of water pollution has become more and more serious. The common waterborne bacteria of *Vibrio cholera*, *E. coli* (*E. coli*), and *Shigella flexneri* seriously endanger people's lives and health [39]. Therefore, it is extremely important to establish a timely and accurate detection mechanism. Traditional waterborne bacterial sensors are usually based on wavelength modulation, and most of the media have dispersion characteristics, even if the dispersion characteristics are very weak, but for high-precision biosensors, such dispersion features are not negligible. Therefore, in order to avoid this shortcoming, we try to design biosensors in the angle domain. If the jump features near the ENZ frequency can be transferred to the angle domain, it will be interesting to apply these fragile jump characteristics to carry through the analysis of unknown objects.

In this paper, we shift the ENZ jump performances of the ENG materials from the frequency domain to the spatial domain and comply with a high-throughput convertible angle selection transparent window. No matter whether the TE wave or the TM wave is incident, the excellent narrow-band SS properties can be achieved. By continuously adjusting the electronic plasma frequency and pushing the refractive index measurement range of the object to be measured to the linear area, multi-segment measurement can be completed, which gives impetus to the possibility of flexibly broadening the range of the sensor. The detection of *Vibrio cholera*, *E. coli*, and *Shigella flexneri* has also been carefully premeditated. We hope that the proposed structure can provide a new idea for SS device design, which is different from the previous hundreds of layers of periodic stack structure, and provides the possibility for highly sensitive sensor design.

2. Structure design and simulation

The schematic diagram of the submitted SS structure is depicted in figure 1. Structure 1 is a single-layer ENG film structure, which utilizes the ENZ resonance to execute high-efficiency SS potentiality, whereas the resonance of the film itself will attenuate the selective performance near the critical angle. Consequently, additional anti-reflection layers need to be added to improve the transmission performance, as described in structure 2. In the anti-reflective layers, the selection of ENG layers with different thicknesses is taken into account. When the electronic plasma frequency changes, the ENG₂ layer of the main structure and the ENG₁ layer of the anti-reflection layers will be adjusted synchronously, which is beneficial to maintaining a larger SS range. The thickness of the lossless dielectric A layer is $d_A = 0.005 d$, and the refractive index is approximately $n_A = 1.35$, where, d is a normalized constant, and its value does not affect the final result [40]. In order to pursue a more optimized theoretical effect, we do not give the specific substance name of medium A here, only the refractive index. These materials can be synthesized by searching in nature or artificial synthesis, which is also a common research method of layered topology [20]. Considering that ENG materials can only be applied in the gigahertz band, the value of the normalized constant d adopted by us should eventually cause the frequency to fall around this range. For ENG materials, the thicknesses are $d_1 = 0.03 d$ and $d_2 = 0.5 d$, and their permeability and permittivity can be expressed as follows [24, 28, 30, 40]:

$$\mu = \mu_1, \quad \varepsilon = \varepsilon_1 - \frac{\omega_p^2}{\omega^2}, \quad (1)$$

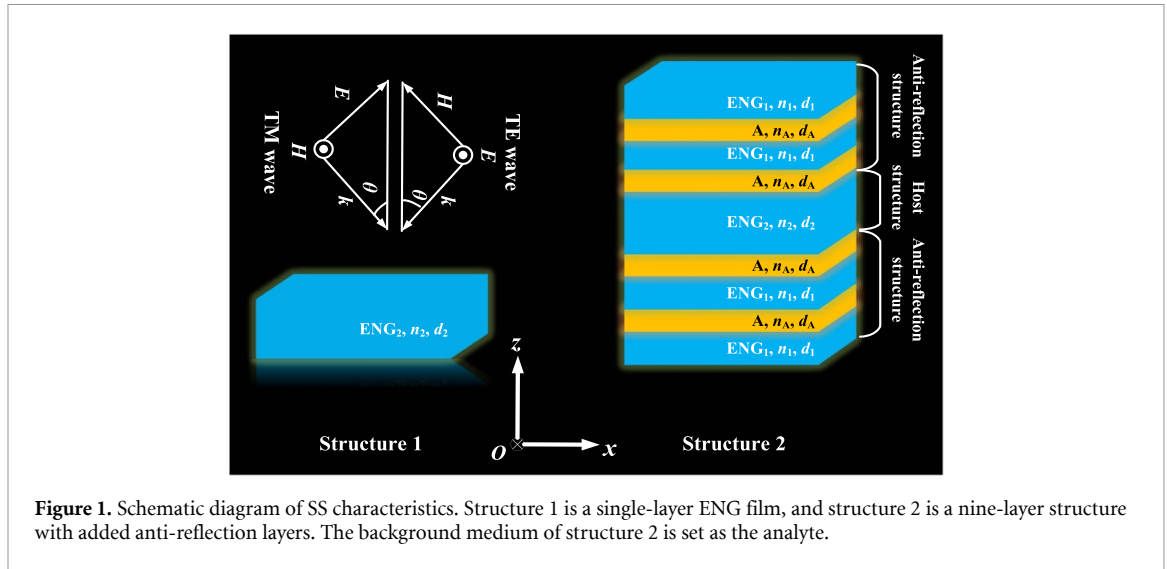


Figure 1. Schematic diagram of SS characteristics. Structure 1 is a single-layer ENG film, and structure 2 is a nine-layer structure with added anti-reflection layers. The background medium of structure 2 is set as the analyte.

where, ω_{ep} is the electronic plasma frequency and ω is the angular frequency, in units of gigahertz. This dispersion model can be implemented in metamaterials utilizing transmission lines by periodically loading lumped elements series capacitors and parallel inductors, and ω_{ep} can be adjusted arbitrarily [25, 28, 40]. In our structure, $\epsilon_1 = 1$, $\mu_1 = 3$, $\omega_{ep} = 30.1 \text{ c d}^{-1}$, $c = 3 \times 10^8 \text{ m s}^{-1}$ [24, 28, 30]. The ENG₁ and ENG₂ layers have the same permittivity and permeability, but their thicknesses are different.

The connection between different media layers is achieved through the transfer matrix method [41] as follows,

$$M = \begin{bmatrix} M_{11} & M_{12} \\ M_{21} & M_{22} \end{bmatrix} = \prod M_i. \tag{2}$$

The transfer matrix of each layer can be determined by the following forms:

$$M_i = \begin{bmatrix} \cos \delta_i & -jp_i^{-1} \sin \delta_i \\ -jp_i \sin \delta_i & \cos \delta_i \end{bmatrix}. \tag{3}$$

Among them, $\delta_i = (2\pi/\lambda) n_i d_i \cos \theta_i$, where $\lambda = 2\pi c/\omega$, $p_i = \sqrt{\epsilon_0/\mu_0} n_i \cos \theta_i$ (TE wave), or $p_i = \sqrt{\epsilon_0/\mu_0} n_i / \cos \theta_i$ (TM wave). θ_i indicates the propagation angle within the i -th layer.

The reflection coefficient r and transmission coefficient t can be written as:

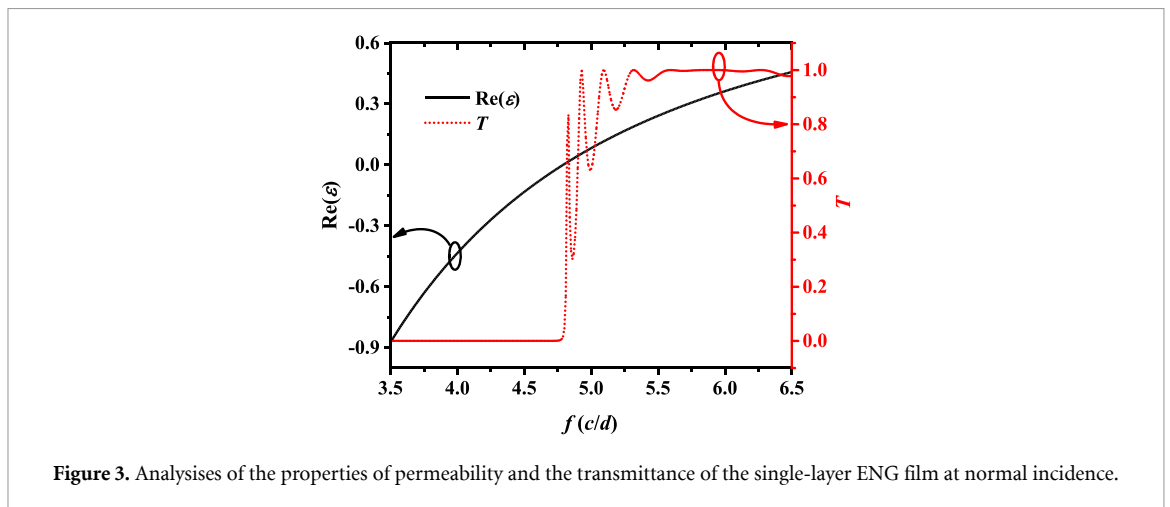
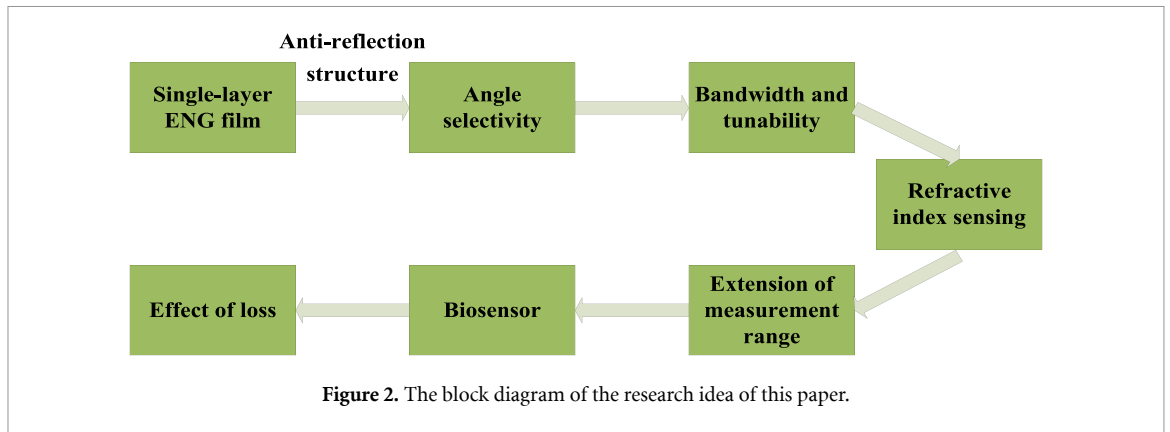
$$r = \frac{(M_{11} + M_{12}p_0)p_0 - (M_{21} + M_{22}p_0)}{(M_{11} + M_{12}p_0)p_0 + (M_{21} + M_{22}p_0)}. \tag{4}$$

$$t = \frac{2p_0}{(M_{11} + M_{12}p_0)p_0 + (M_{21} + M_{22}p_0)}. \tag{5}$$

The reflectance R and transmittance T can be expressed as below:

$$\begin{aligned} R &= |r|^2. \\ T &= |t|^2. \end{aligned} \tag{6}$$

In addition, figure 2 shows the research idea of this paper for easy understanding. Firstly, the selectivity property of monolayer ENG film is studied in the frequency domain. Then, the selection feature is introduced into the angle domain, and the anti-reflection structure is introduced to realize the high flux angle window. Then, the frequency bandwidth and tunability of angle selection are studied. Then, the refractive index sensor is designed based on the edge characteristics of the angle window. Then, the measurement range of the sensor is expanded by changing the electronic plasma frequency. Then, using the high sensitivity of the sensor, the detection of water-borne bacteria is realized. Finally, the effects of loss on the performance of the devices are considered.



3. Analysis and discussion

3.1. A. Analysis of SS performance

In this part, $\omega_{ep} = 30.1 \text{ c d}^{-1}$. In figure 3, the analysis of the properties of permeability and the transmittance of the single-layer ENG film at normal incidence are revealed. When the real part of the permittivity of ENG material is greater than 0, most of the incident energy can pass through the ENG film structure. However, when approaching the ENZ frequency of 4.8 c d^{-1} , the energy propagation will be interrupted and almost all the energy will be reflected, and this phenomenon is maintained when permittivity is negative.

Similarly, since the ENZ jump property can be implemented in the frequency domain, it will also exist in the spatial angle domain. In figure 4, the incident frequency is fixed at $f = 5.5 \text{ c d}^{-1}$, and the SS feature with high flux is independent of the polarization characteristic, and the impedance matching and energy distribution are also studied. To display the filtering performance of SS structure more intuitively, we define the SF as the ratio of the angle range with a transmittance of -3 dB to that with a transmittance of -30 dB [42]:

$$\text{SF} = \frac{\Delta\theta_{-3\text{dB}}}{\Delta\theta_{-30\text{dB}}}. \quad (7)$$

Monolayer ENG film can certainly form a large-angle transmission window to a certain extent. However, in view of the resonance defect of the monolayer film itself, a small range of transmission gap will be formed near the critical angle, which damages the SS performance. Therefore, it is necessary to introduce appropriate anti-reflection structures to offset the harm brought by the monolayer film resonance. The replenished anti-reflection coatings themselves will also produce resonance, but when the two are resonating together, if the conditions for interference cancellation are satisfied in phase, then the original transmission gap will be filled. At the same time, the addition of auxiliary structures does not affect the initial SS range. In line with the comparison of figures 4(a) and (b), under different polarization states, the transmission performances have been significantly improved after the introduction of anti-reflection layers, which is better than 0.9. For the TE wave, the SS phenomenon involves $0\text{--}56.3$ degrees, while in the case of the TM one, the covered SS

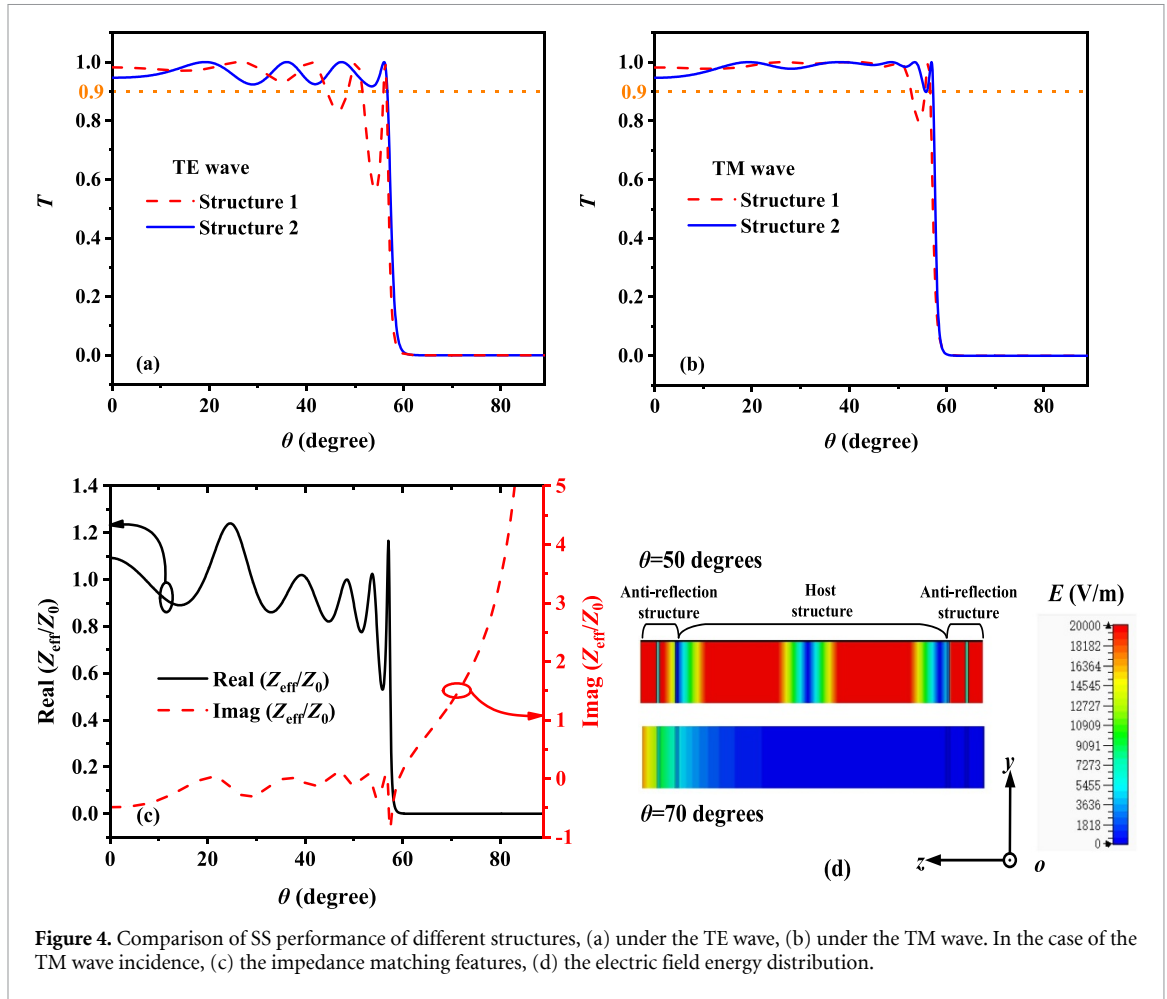


Figure 4. Comparison of SS performance of different structures, (a) under the TE wave, (b) under the TM wave. In the case of the TM wave incidence, (c) the impedance matching features, (d) the electric field energy distribution.

range is 0–57 degrees, and the SFs of both are higher than 0.9. Slightly different, in the high-flux selection range, there is a difference in flatness between the TE and TM waves, which is caused by the different electromagnetic responses of different polarization states to incident angles. In the derivation of admittance, the former is proportional to the cosine of the incident angle, while the latter is inversely proportional [41].

To characterize the propagation performance more convincingly, we introduce the concept of normalized surface effective impedance [42]. The normalized effective surface impedance can be defined by the ratio of the effective surface impedance of the structure ($Z_{\text{eff}} = |E|/|H| = \sqrt{\mu/\varepsilon}$) to the vacuum wave impedance ($Z_0 = |E_0|/|H_0| = \sqrt{\mu_0/\varepsilon_0}$).

$$\frac{Z_{\text{eff}}}{Z_0} = z_{r,\text{eff}} + jz_{i,\text{eff}} = \frac{1+r}{1-r}. \quad (8)$$

When the real part of the effective impedance of the normalized surface approaches 1 while the imaginary part tends to 0, the effective impedance of the overall structure is fully matched with the free space wave impedance, which can fully inhibit reflection. On the contrary, it means that the two are completely mismatched, and electromagnetic waves cannot penetrate the structure. Here, we only analyze the incident situation of the TM wave in structure 2, and that of the TE one will be similar. In figure 4(c), $\text{Real}(Z_{\text{eff}}/Z_0)$ retains a high level with significant impedance matching in the area lower than 57 degrees, and $\text{Imag}(Z_{\text{eff}}/Z_0)$ tends to 0 in the same area, with complete impedance matching features and energy transmission process contained. At the same time, the electric field energy distribution in figure 4(d) can also prove this point very well. We set the intensity of the incident electric field as unity $|E_{\text{in}}| = 1$. When the incident angle is 50 degrees, the electric field distribution of the whole structure is very strong, which means that the electromagnetic wave penetrates the whole structure, so the transmission energy is very high, and when the incident angle is 70 degrees, the electromagnetic wave is very weakly distributed at the beginning of the structure, which shows that electromagnetic waves are reflected out without entering the structure at all.

The single-frequency SS structure is limited in practical applications, and it is imperative to expand the frequency range as much as possible. As mentioned earlier, the added anti-reflection coatings contain the ENG layers, so the frequency shift will simultaneously regulate ENG_1 and ENG_2 , which is conducive to

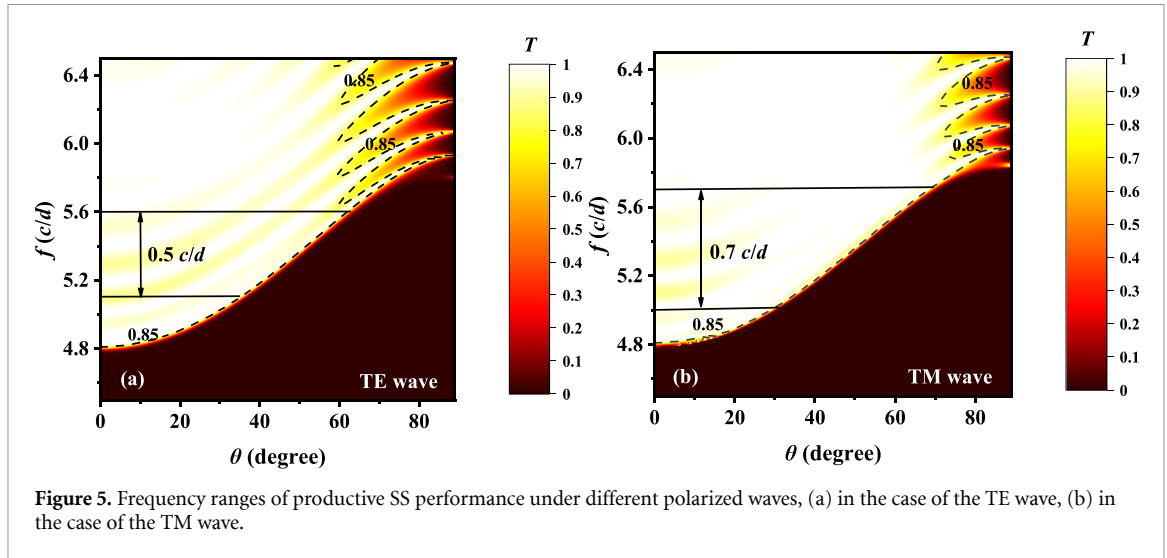


Figure 5. Frequency ranges of productive SS performance under different polarized waves, (a) in the case of the TE wave, (b) in the case of the TM wave.

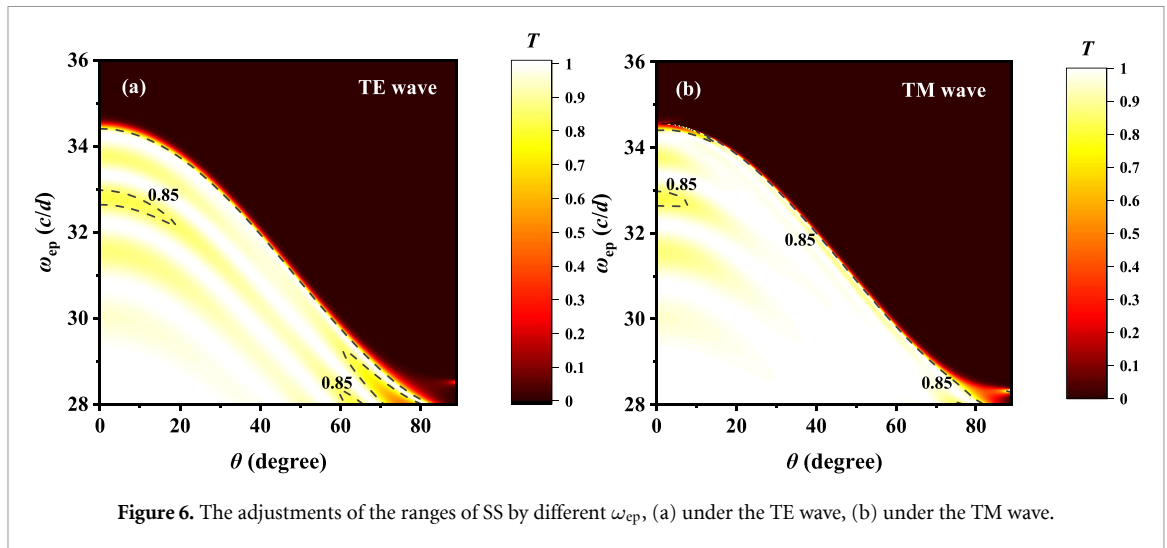


Figure 6. The adjustments of the ranges of SS by different ω_{ep} , (a) under the TE wave, (b) under the TM wave.

achieving dynamic balance within a certain frequency range and expanding the range of impedance matching. For the sake of enhancing the intuitive effect of visualization, the area where the transmittance exceeds 0.85 and the SF surpasses 0.9 is specified as the SS that meets the requirements. The frequency ranges of productive SS performance under different polarized waves are shown in figure 5. As for the TE wave in figure 5(a), effective SS performance is satisfied within the range of incident frequency of 5.1–5.6 $c d^{-1}$, and the bandwidth is 0.5 $c d^{-1}$. Concurrently, under the condition of the TM wave in figure 5(b), the corresponding frequency domain is 5–5.7 $c d^{-1}$, resulting in a bandwidth of 0.7 $c d^{-1}$. Overall, the SS behavior under the TM wave is slightly stronger than the TE one.

For convenience, $f = 5.5 c d^{-1}$ is still referred for investigation. The adjustments of the ranges of SS by different ω_{ep} are illustrated in figure 6. In the case of the TE wave incidence in figure 6(a), with the expansion of ω_{ep} , the scope of SS has an obvious trend of narrowing. When ω_{ep} is less than 29.3 $c d^{-1}$ or in the range of 32.2 $c d^{-1}$ –33 $c d^{-1}$, there are transmission defects in the area of large angle or small angle, respectively, so that the transmittance is lower than 0.85, and if ω_{ep} is higher than 34.3 $c d^{-1}$, SS phenomenon disappears. Likewise, a similar effect exists when the TM wave propagates in figure 6(b). Different degrees of large-angle or small-angle transmission gaps appear in the regions below 28.1 $c d^{-1}$ or 32.6–33 $c d^{-1}$ and 34.1–34.5 $c d^{-1}$, respectively, and in the case of ω_{ep} above 34.5 $c d^{-1}$, the SS performance is destroyed.

3.2. Potential of SS capability in refractive index sensing and biosensing

In traditional studies, analyte cavities are usually located in one or several layers of the structure, and the fact that analytes are only a few hundred nanometers or a few microns in size presents practical operation risks. Remarkably, in the proposed structure, we set the background medium as the object to be measured, which

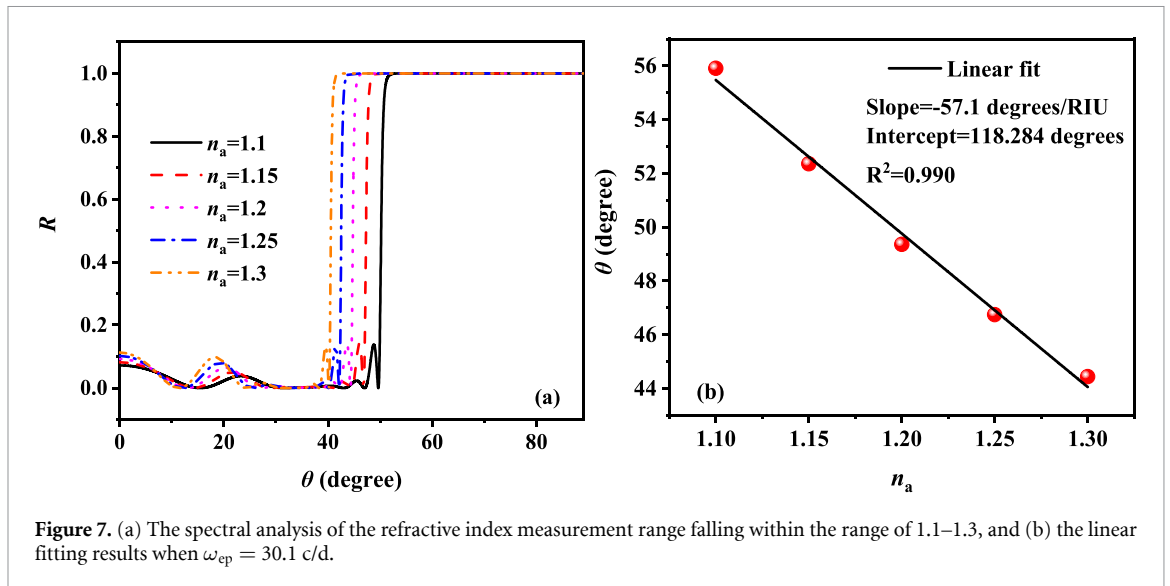


Figure 7. (a) The spectral analysis of the refractive index measurement range falling within the range of 1.1–1.3, and (b) the linear fitting results when $\omega_{ep} = 30.1$ c/d.

greatly reduces the complexity of actual processing. The position of the critical angle of ENZ characteristics strongly depends on the difference in the external medium, which provides the possibility for new measurement methods. To enhance the readability and visualization of the sensor and avoid harmonic interference, the reflectivity critical angle is selected for observation. When the composition of the analyte is a certain value, the reflectivity will drop rapidly at the corresponding critical angle and the energy will be transmitted. The case of the TM wave incidence is used for sensing analysis. For the sake of enhancing the visualization, we define the jump point where the reflectivity decreases from 1 as the sensor detection point.

The analysis of the refractive index measurement range falling within the range of 1.1–1.3 is revealed in figure 7. In figure 7(a), if the refractive index of the analyte n_a increases from 1.1 to 1.3 with intervals of 0.05, the critical angles are 55.91 degrees, 52.36 degrees, 49.36 degrees, 46.75 degrees, and 44.44 degrees. In figure 7(b), it can be seen from the linear fitting relationship that the sensitivity can reach 57.1 degrees/RIU and the R^2 of the characterization accuracy is equal to 0.990, which is conducive to high-precision refractive index resolution. Intercept refers to the ordinate of the intersection of the fitting equation of the analyte with the vertical axis. However, if the refractive index of the analyte is higher than 1.3 or lower than 1.1, the linearity of the sensing structure will be sacrificed to a large extent, which is not beneficial to the high-precision measurement. Resultantly, ω_{ep} needs to be adjusted to make the proposed structure return to the linear region, so as to achieve the purpose of expanding the range.

In figure 8, by regulating ω_{ep} , thereby forcing the sensor structure to return to the linear region, the intention of measuring the high refractive index analyte is fulfilled. As observed in figures 8(a)–(c), when ω_{ep} is changed to 28 c d^{-1} , 26 c d^{-1} , or 24 c d^{-1} respectively, the measurement range advances to 1.3–1.5, 1.5–1.7, or 1.7–1.9. The sensitivity decreased significantly, being 48.8 degrees/RIU, 40 degrees/RIU, and 32.8 degrees/RIU, respectively, while the accuracy level remains at a high level all the time, and R^2 values exceed 0.992. It can be seen that by using the lubrication effect of ω_{ep} , the linear area can be continuously regulated, accomplishing the sake of expanding the measurement range. Figure 8 only exhibits the range of 3 sections and the measurement range will be further expanded if the reasonable regulation of ω_{ep} is continued.

For the proposed SS angle sensor, the resolution of the sensor is largely determined by the size of the SF. The higher the SF is, the stronger the ability to detect the lowest refractive index difference is. The ENG_2 layer is the key to determining the SS capability, so it is necessary to explore the effect of its thickness on the SF. For the purpose of showing universality, the situation when the background medium is air is analyzed. The influences of different thicknesses on the SF, and the detection of three different waterborne bacteria are represented in figure 9. In figure 9(a), it is obvious that as d_2 increases, the SF increases significantly. If d_2 is equal to 0.5 c d^{-1} , 1.0 c d^{-1} or 1.5 c d^{-1} , the SF is 0.978, 0.993, or 0.997. Significantly, the enhancement of d_2 is conducive to the consolidation of the SF, and it also enhances the resolution of the sensor. However, it is worth emphasizing that the augmentation in thickness will also raise the resonance near the critical angle. When d_2 is 1.5 c d^{-1} , a resonance gap exceeding 0.6 is produced. If the thickness continues to increase, the sensing performance may be affected. Therefore, the choice of thickness also needs to consider the actual application situation, and the thickness cannot be increased blindly in exchange for the increase of the SF. Taking into account the requirements for the refractive index resolving power of waterborne bacteria,

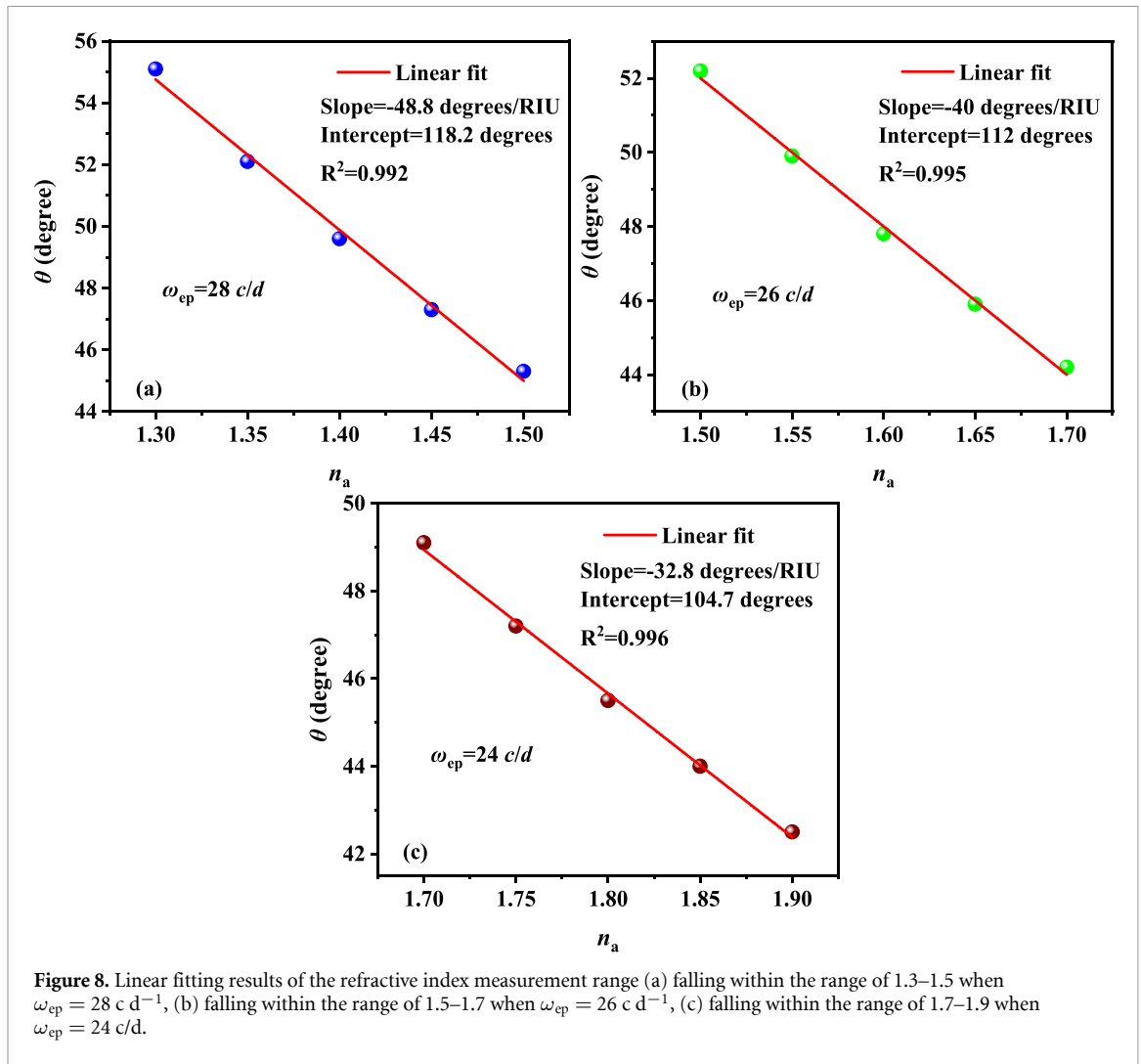


Figure 8. Linear fitting results of the refractive index measurement range (a) falling within the range of 1.3–1.5 when $\omega_{ep} = 28 \text{ c d}^{-1}$, (b) falling within the range of 1.5–1.7 when $\omega_{ep} = 26 \text{ c d}^{-1}$, (c) falling within the range of 1.7–1.9 when $\omega_{ep} = 24 \text{ c/d}$.

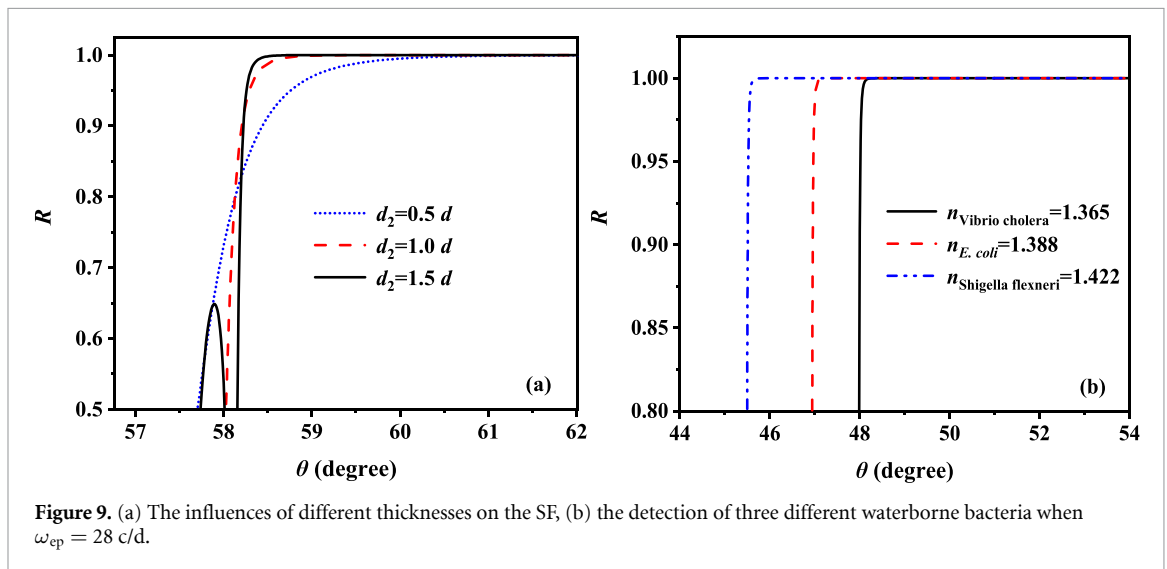
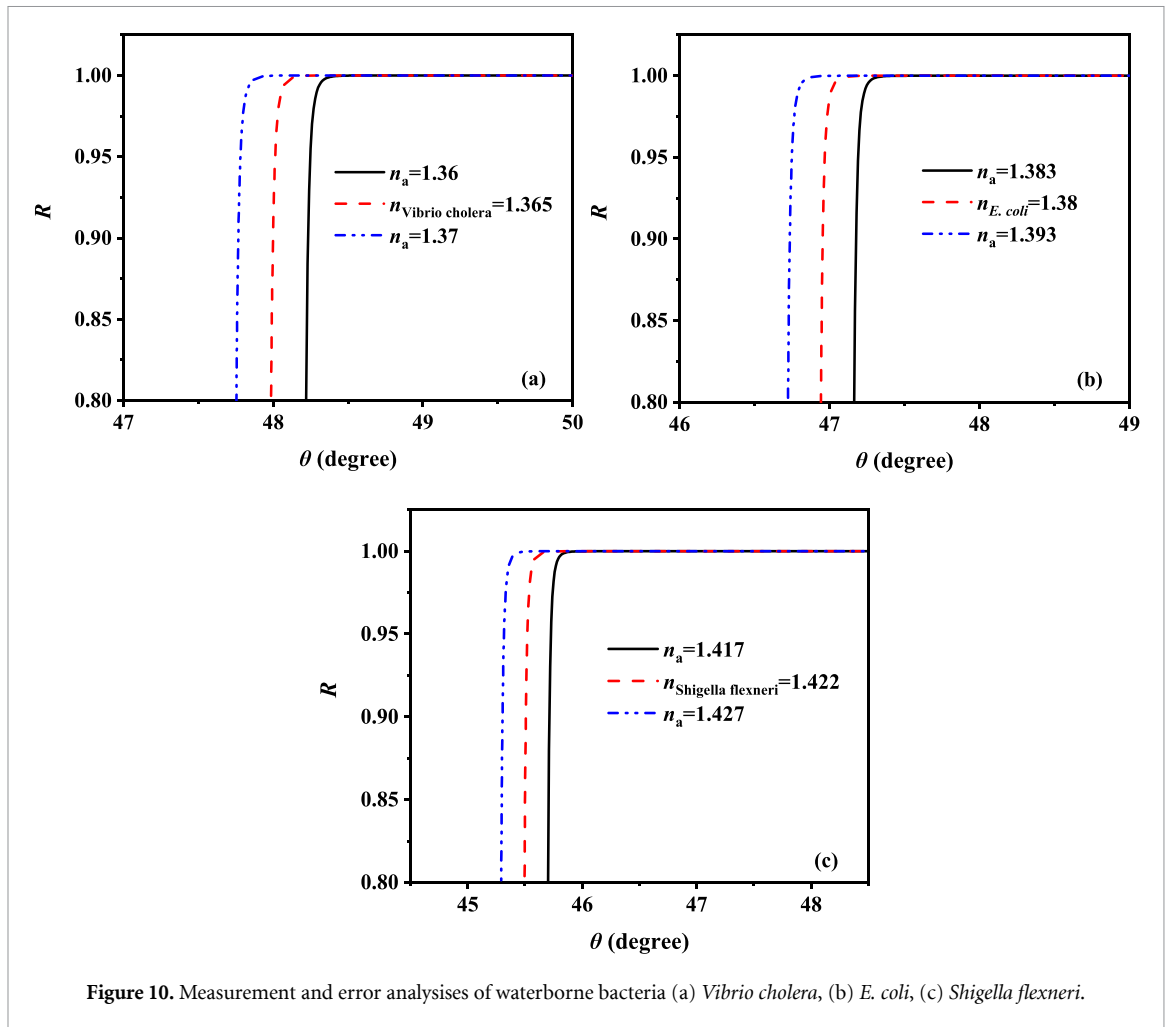


Figure 9. (a) The influences of different thicknesses on the SF, (b) the detection of three different waterborne bacteria when $\omega_{ep} = 28 \text{ c/d}$.

$d_2 = 1.5 \text{ c d}^{-1}$ is adopted. It can be seen from figure 9(b) that when the position of the analyte is filled with *Vibrio cholera*, *E. coli*, or *Shigella flexneri* [39], the corresponding critical angle position is converted to 48.49 degrees, 47.39 degrees, or 45.93 degrees, which is uncomplicated to distinguish.



According to [35], when the resolving power of the sensor reaches 0.005, these three types of waterborne bacteria can be accurately differentiated. Measurement and error analysis of waterborne bacteria are shown in figure 10. In figure 10(a), when the refractive index error of *Vibrio cholera* is -0.005 , 0 , or 0.005 , the corresponding critical angle position is 48.69 degrees, 48.46 degrees, or 48.22 degrees, and the angle differences between the front and back are 0.23 degrees and 0.24 degrees. In figure 10(b), the corresponding critical angle position is 47.62 degrees, 47.39 degrees, or 47.17 degrees, with differences of 0.23 degrees and 0.22 degrees. In figure 10(c), the corresponding value is 46.13 degrees, 45.93 degrees, or 45.72 degrees, and the angle differences are 0.2 degrees and 0.21 degrees. From the above analysis, it can be observed that the designed sensor structure is fully capable of the refractive index difference of 0.005, so it is more than adequate for the measurement of the three water-borne bacteria.

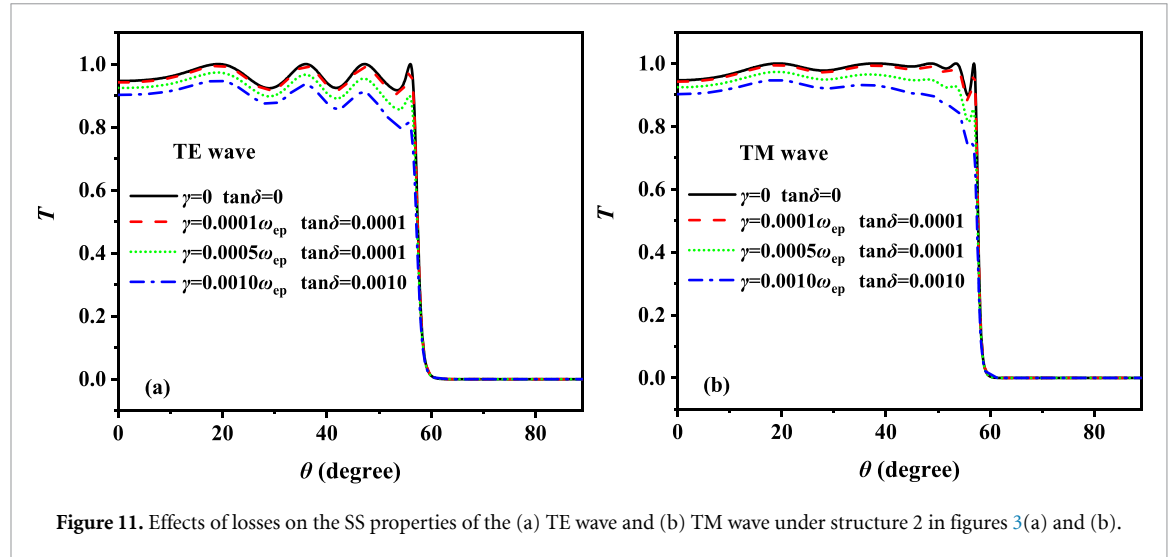
Considering that there may be errors in the thickness of the medium in the actual manufacturing process, the concept of tolerance coefficient is introduced here for analysis. The tolerance coefficient refers to the proportional deviation of all media based on the original thickness. For the convenience of elaboration, three biological indicators are used for analysis. We know that the three bacteria can be identified within the refractive index error of 0.005 or less, which means that they can be judged within a certain range of angles, as shown in figure 10 of the manuscript. Therefore, as long as the jump angle is still within the error range, the tolerance coefficient value will not affect the identification of biological indicators. Table 1 shows tolerance ranges for the three biological indicators.

3.3. Analysis of the effects of losses on SS devices and sensing devices

To pursue the theoretical optimal effect, we do not consider the loss effect of the medium above. However, previous experimental results show that the Drude model can better fit the optical properties of ENG materials [29], so here we analyze the lossy form of ENG materials, and the loss tangent of medium A is also taken into account. In the previous study, we adopt a normalization method. When we set the normalization

Table 1. Thickness tolerance coefficient of the medium in the z-direction of the propagation direction.

Analyte	Angle		Tolerance coefficient	
	Standard value (degrees)	Margin of error (degrees)	Standard value	Margin of error
Vibrio cholera	48.46	48.69 ~ 48.22	1	0.8 ~ 1.51
<i>E. coli</i>	47.39	47.62 ~ 47.17	1	0.8 ~ 1.5
<i>Shigella flexneri</i>	45.93	46.13 ~ 45.72	1	0.8 ~ 1.49

**Figure 11.** Effects of losses on the SS properties of the (a) TE wave and (b) TM wave under structure 2 in figures 3(a) and (b).

constant d to be 0.903 m, the frequency f is 1.8272 GHz, the electric damping factor γ is 1 MHz, and the ω_{ep} is 10 GHz. These values are consistent with the values in [29]. And at this time, the relationship of $\gamma = 0001\omega_{ep}$ is satisfied. Other parameters remain the same as above.

$$\mu = \mu_1, \quad \varepsilon = \varepsilon_1 - \frac{\omega_{ep}^2}{\omega^2 - i\omega\gamma}. \quad (9)$$

First, the impacts of losses on the SS characteristics are explored. To reflect the comprehensiveness of the study, we not only consider the losses situation in [29], but also investigate the effects of appropriate changes in losses on SS performance. For the convenience of the discussion, the TE and TM waves in the case of structure 2 in figures 3(a) and (b) are chosen to be discussed respectively as typical. In figures 11(a) and (b), we compare the cases of $\gamma = 0.0001\omega_{ep}$ and $\tan\delta = 0.0001$, $\gamma = 0.0005\omega_{ep}$ and $\tan\delta = 0.0005$, and $\gamma = 0.001\omega_{ep}$ and $\tan\delta = 0.001$ with $\gamma = 0$ and $\tan\delta = 0$, respectively. The results show that, whether it is a TE wave or TM wave, with the increase of γ and $\tan\delta$, the dielectric losses will cause the energy to be absorbed by the structure, so the transmission performance will decrease, but the approximate angular range does not produce a significant shift. If the losses are further increased, worse transmission performance will be obtained, which is not ideal. Therefore, we hope that the losses can be reduced as much as possible in the process of experimental processing.

We also inspect the influences of losses on sensor performance. Two typical representatives in figure 7(a), $n_a = 1.1$ and $n_a = 1.3$, are selected as test subjects, and the situations are similar for other analytes. In figures 12(a) and (b), the same γ and ω_{ep} as in figure 11 are set up for analysis. Similarly, the enhancement of losses will worsen the reflection window used for sensing. The part with a reflectivity higher than 0.8 will be significantly offset, while the part with a reflectivity lower than 0.8 will be slightly threatened by losses. In the above discussion, we set the sensor detection point as the point where the reflectivity jumps from 1, which is not applicable here. If we adjust the detection point to a reflectivity of 0.5, the effects of losses will be greatly attenuated without affecting the basic performance of the sensor.

To highlight the advantages of the proposed design method in expanding the measurement range of the refractive index sensor, table 2 is shown.

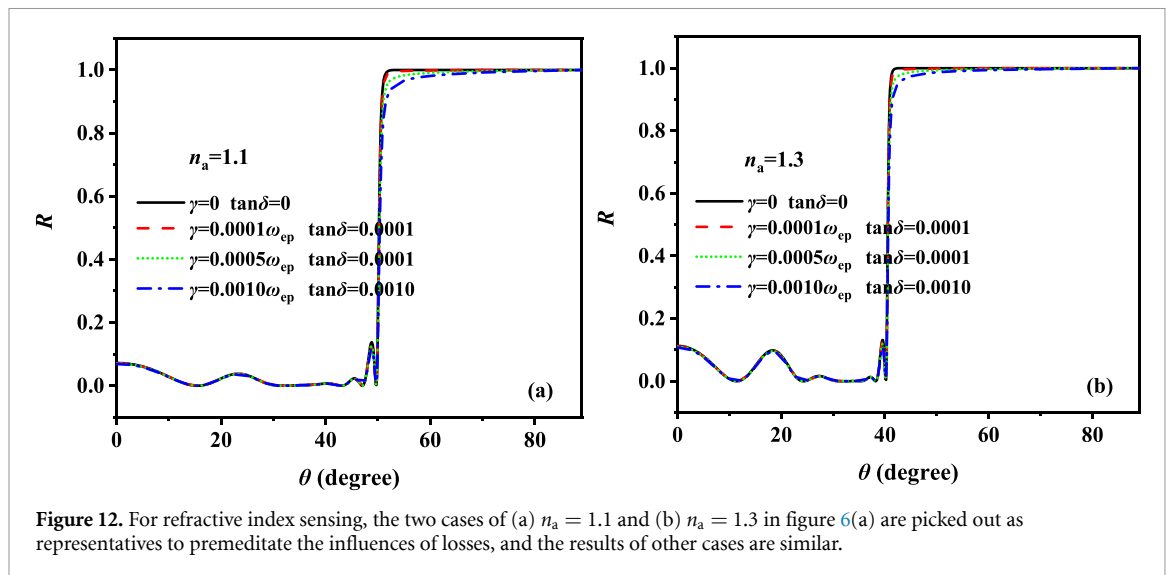


Figure 12. For refractive index sensing, the two cases of (a) $n_a = 1.1$ and (b) $n_a = 1.3$ in figure 6(a) are picked out as representatives to premeditate the influences of losses, and the results of other cases are similar.

Table 2. The comparison of the proposed refractive index sensor with previous work.

References	Principle	Measurement range (RIU)	Maximum sensitivity (degrees/RIU)
[32]	Surface plasmon resonance	1.33–1.335	129.84
[43]	Bloch surface waves	1.33–1.34	25.1
[44]	Lossy mode resonance	1.33–1.45	61.922
[45]	Surface plasmon resonance	1.33–1.336	175
[46]	Tamm state	1.333–1.33862	21.89
This work	ENZ spatial selection	1.1–1.9	57.1

4. Conclusion

In summary, we use the ENZ characteristics of ENG materials to achieve high-throughput and polarization-independent SS performance with only a 9-layer structure, which is different from the previous dozens of layers of periodic stack structure. For the TE and TM waves, the SS ranges are $5.1\text{--}5.6 \text{ c d}^{-1}$ and $5.0\text{--}5.7 \text{ c d}^{-1}$. If the background medium is set as the analyte, multi-stage refractive index measurement can be accomplished by continuously adjusting ω_{ep} to make the overall structure return to the linear region. When the analyte with the measurement range is 1.1–1.3, 1.3–1.5, 1.5–1.7, or 1.7–1.9, the corresponding sensitivity is 57.1 degrees/RIU, 48.8 degrees/RIU, 40 degrees/RIU, or 32.8 degrees/RIU. In addition, the increase of d_2 is conducive to the enhancement of the SF, to attain the detection of the three types of waterborne bacteria *Vibrio cholera*, *E. coli*, and *Shigella flexneri*.

Data availability statement

The data generated and/or analysed during the current study are not publicly available for legal/ethical reasons but are available from the corresponding author on reasonable request.

ORCID iD

Haifeng Zhang  <https://orcid.org/0000-0002-9890-8345>

References

- [1] Nguyen H C, Hashimoto S, Shinkawa M and Baba T 2012 *Opt. Express* **20** 22465
- [2] Zayats A V, Smolyaninov I I and Maradudin A A 2005 *Phys. Rep.* **408** 131
- [3] Berini P 2009 *Adv. Opt. Photonics* **1** 484
- [4] Maigyte L and Staliunas K 2015 *Appl. Phys. Rev.* **2** 011102
- [5] Shen Y, Hsu C W, Yeng Y X, Joannopoulos J D and Soljačić M 2016 *Appl. Phys. Rev.* **3** 011103
- [6] Liang G, Han P and Wang H 2004 *Opt. Lett.* **29** 192

- [7] Maigyte L, Gertus T, Peckus M, Trull J, Cojocaru C, Sirutkaitis V and Staliunas K 2010 *Phys. Rev. A* **82** 043819
- [8] Purlys V, Maigyte L, Gailevičius D, Peckus M, Malinauskas M and Staliunas K 2013 *Phys. Rev. A* **87** 033805
- [9] Nagashima K, Tsubouchi M, Och Y and Maruyama M 2018 *J. Appl. Phys.* **123** 123104
- [10] Grineviciute L, Babayigit C, Gailevičius D, Bor E, Turdnev M, Purlys V, Tolenis T, Kurt H and Staliunas K 2019 *Appl. Surf. Sci.* **481** 353
- [11] Luo Z, Tang Z, Xiang Y, Luo H and Wen S 2009 *Appl. Phys. B* **94** 641
- [12] Shen Y C, Ye D X, Wang L, Celanovic I and Ran L X 2014 *Phys. Rev. B* **90** 125422
- [13] Colak E, Cakmak A O, Serebryannikov A E and Ozbay E 2010 *J. Appl. Phys.* **108** 113106
- [14] Alu A, Aguanno G D, Mattiucci N and Bloemer M J 2011 *Phys. Rev. Lett.* **106** 123902
- [15] Akozbek N, Mattiucci N, Ceglia D, Trimm R, Alù A, D'Aguanno G, Vincenti M A, Scalora M and Bloemer M J 2021 *Phys. Rev. B* **85** 635
- [16] Iizuka H, Engheta N and Sugiura S 2016 *Opt. Lett.* **41** 3829–32
- [17] Yao Z N, Luo J and Lai Y 2016 *Opt. Lett.* **41** 5106–9
- [18] Li S S, Wang Y, Zhang W Y, Lu W X, Hou B, Luo J and Lai Y 2020 *New J. Phys.* **22** 023033
- [19] Wu F, Long Y, Li H J, Chen Y, Pan M Y and Wu X H 2021 *Appl. Opt.* **60** 2811
- [20] Shen Y, Ye D, Celanovic I, Johnson S G, Joannopoulos J D and Soljačić M 2014 *Science* **343** 1499
- [21] Tanaka H, Takai I, Fujikawa H and Iizuka H 2018 *J. Lightwave Technol.* **36** 2517
- [22] Qu Y R, Shen Y C, Yi K Z, Yang Y Q, Li Q, Qiu M and Soljačić M 2018 *ACS Photonics* **5** 4125
- [23] Grineviciute L, Babayigit C, Gailevičius D, Peckus M and Staliunas K 2020 *Adv. Opt. Mater.* **9** 2001730
- [24] Wang L G, Chen H and Zhu S Y 2004 *Phys. Rev. B* **70** 245102
- [25] Liu J D, Liu S B, Kong X K and Dai Y 2014 *Eur. Phys. J.* **66** 30102
- [26] Thapa K B, Pandey P C, Singh P P and Ojha S P 2013 *Optik* **124** 6631
- [27] Li H, Zhang Y, Zhang L, He L, Li H and Chen H 2007 *J. Appl. Phys.* **102** 033711
- [28] Jiang H, Chen H, Li H, Zhang Y, Zi J and Zhu S 2004 *Phys. Rev. E* **69** 066607
- [29] Chen Y H 2010 *Opt. Express* **18** 130343
- [30] Chen Y H, Wang X G, Yong Z H, Zhang Y J, Chen Z F, He L X, Lee P F, Chan H L W, Leung C W and Wang Y 2012 *Phys. Lett. A* **376** 1396
- [31] Ma G, Liang R, Wan Z and Wang S 2021 *Nat. Commun.* **12** 3365
- [32] Dai L M, Xiang X Y, Jia Y J, Jiang Y and Guo L Y 2017 *J. Lightwave Technol.* **35** 82
- [33] Srivastava S K, Arora V, Sapra S and Gupta B D 2012 *Plasmonics* **7** 261
- [34] Shalabney A and Abdulhalim I 2011 *Laser Photonics. Rev.* **5** 571
- [35] Salah H B, Hocini A, Temmar M N and Khedrouche D 2019 *Chin. J. Phys.* **61** 86
- [36] Salah H B, Hocini A, Bahri H and Melouki N 2021 *ECS J. Solid State Sci. Technol.* **10** 081001
- [37] Salah H B, Hocini A, Bahri H, Khedrouche D, Ingebrandt S and Pachauri V 2022 *J. Opt.* **193** 1–12
- [38] Hocini A, Salah H B and Temmar M N E 2021 *J. Comput. Electron.* **20** 1354
- [39] Liu P Y, Chin L K, Ser W, Ayi T C, Yap P H, Bourouinad T and Leprince-Wang Y 2014 *Lab Chip* **14** 4237
- [40] Eleftheriades G V, Iyer A K and Kremer P C 2002 *IEEE Trans. Microw. Theory Tech.* **50** 2702
- [41] Qi L M, Yang Z Q, Lan F, Gao X and Shi Z J 2010 *Phys. Plasmas* **17** 042501
- [42] Wan B F, Zhang H F and Wang P X 2021 *Opt. Lett.* **46** 1934
- [43] Zou X J, Zheng G G and Chen Y Y 2018 *Chin. Phys. B* **27** 6
- [44] Saini R, Kumar A, Bhatt G, Kapoor A, Paliwal A, Tomar M and Gupta V 2020 *IEEE Sens. J.* **20** 1217–22
- [45] Zhao Y T, Gan S W, Zhang G H and Dai X Y 2019 *Results Phys.* **14** 102477
- [46] Belotelov V 2021 *Sensors* **21** 1984